Chapter 5 Radiative Properties of Clouds

Michael D. King
NASA Goddard Space Flight Center
Greenbelt, Maryland

This paper presents an overview of our current understanding of the radiative properties of clouds, placing particular emphasis on recent results and unanswered problems arising from the marine stratocumulus and cirrus cloud components of the First ISCCP (International Satellite Cloud Climatology Project) Regional Experiment (FIRE), conducted in the United States during 1986 and 1987. For marine stratocumulus clouds, we present and discuss the discrepancy between observations and theory of the absorption of solar radiation by clouds, the discrepancy between remote sensing and *in situ* estimates of the effective droplet radius derived from spectral reflectance measurements, and the variability and spatial structure of stratocumulus clouds derived from both reflection and transmission measurements. We will describe the thermal emission characteristics of cirrus clouds and will demonstrate how the brightness temperature difference in the split-window region of the thermal infrared can be used to infer the effective radius of ice crystals, observations that lead to the conclusion that ice crystals are much smaller than previously believed. We will also illustrate the relationship between thermal emittance and visible albedo that has been derived from airborne observations of cirrus clouds. These results generally show that the thermal emittance of cirrus clouds is less than theoretically predicted for a given value of the visible albedo.

I. Introduction

Clouds vary considerably in their horizontal and vertical extent (Stowe et al., 1989; Rossow et al., 1989), in part due to the circulation pattern of the atmosphere with its requisite updrafts and downdrafts, and in part due to the distribution of oceans and continents and their numerous and varied sources of cloud condensation nuclei (CCN). Clouds strongly modulate the energy balance of the earth and its atmosphere through their interaction with shortwave and longwave radiation,

as demonstrated both from satellite observations (Ramanathan, 1987; Ramanathan et al., 1989) and from modeling studies (Ramanathan et al., 1983; Cess et al., 1989). Of paramount importance to a comprehension of the earth's climate and its response to anthropogenic and natural variability is a knowledge of the radiative, microphysical, and optical properties of clouds.

Marine stratocumulus clouds exert a large influence on the radiation balance of the earth–atmosphere–ocean system through their large aerial extent, temporal persistence, and high reflectivity of solar radiation. Cirrus clouds, on the other hand, exert their greatest radiative influence on the earth's climate through their effect on longwave radiation emitted to space. Both of these cloud types are spatially and temporally persistent in the earth's atmosphere, and both create difficulty in the remote sensing of cloud properties from spaceborne sensors. As a direct consequence of the need to determine the optical and microphysical properties of clouds from present and future spaceborne systems, such as the Moderate Resolution Imaging Spectroradiometer (MODIS; King et al., 1992), a need arose to conduct intensive field observations (IFOs) of marine stratocumulus and cirrus clouds. These two field campaigns, conducted as major components of the First ISCCP Regional Experiment (FIRE; Cox et al., 1987), itself an element of the International Satellite Cloud Climatology Project (ISCCP; Schiffer and Rossow, 1983), has focused exclusively on these two cloud types. Largely as a result of these two field experiments, the radiative and microphysical properties of these cloud systems have been more extensively studied than others.

In this chapter, we summarize the state of our knowledge of the radiative properties of clouds based on these and other experiments that have had an especially profound impact on our understanding of cloud radiative properties. We begin this review by examining the principal observations that have contributed to our knowledge of the absorption of solar radiation by clouds, placing particular emphasis on recent observations and explanations for the widely observed discrepancy between theory and observations, wherein clouds are often observed to absorb more solar radiation than models can explain. In addition, we will describe the status of a number of recent efforts to determine the microphysical and radiative properties of clouds from reflected solar radiation measurements, again focusing on marine stratocumulus observations.

We will also illustrate the spatial variability of the spectral reflectance and the angular transmission characteristics of clouds based on aircraft observations conducted off the coast of Southern California during the marine stratocumulus IFO. For cirrus clouds, we will summarize recent findings on the thermal emission characteristics of these clouds, together with a description of the effective radius of ice crystals inferred from aircraft and satellite observations. Finally, we will describe the relationship between the thermal emittance and visible albedo of cirrus clouds derived from actual field observations.

II. Marine Stratocumulus Clouds

A. Spectral Absorption of Solar Radiation

The absorption of solar radiation by clouds is governed by the optical thickness, single scattering albedo, and phase function of the cloud, as well as the reflectance of the underlying surface and the water vapor distribution of the environment in which the cloud is located. Theoretical calculations suggest that water clouds absorb up to 15–20% of the incident solar radiation, with the largest values arising from the thickest clouds having large cloud droplets, an overhead sun, and little water vapor above the cloud (Twomey, 1976; Slingo and Schrecker, 1982; Davies et al., 1984; Stephens et al., 1984; Wiscombe et al., 1984; Slingo, 1989). In addition to the total cloud absorption, calculations also show that heating rates near cloud top can reach 2 K h^{-1}, thereby contributing significantly to the sudden "burning off" of California stratus layers as the solar zenith angle decreases toward noon (Twomey, 1983).

The majority of cloud absorption observations to date have involved measurements obtained using broadband pyranometers mounted on research aircraft flown above and below clouds. All of the observations thus far reported in the literature have involved single aircraft missions in which it is exceedingly difficult to obtain comparable flux observations above and below the same cloud layer. In spite of these difficulties, aircraft pyranometer observations by Reynolds et al. (1975), Herman (1977), Stephens et al. (1978), Herman and Curry (1984), Hignett (1987), and Foot (1988) have consistently shown a discrepancy between measurements and theory, whereby measurements of the absorption of solar radiation by clouds generally suggest that clouds absorb more solar energy than theoretical predictions can explain for clouds composed solely of liquid water and water vapor.

As a consequence of the reported discrepancies between measurements and theory on the absorption of solar radiation by clouds, recognized by the atmospheric radiation community for more than four decades, a large number of competing hypotheses have been offered to explain this "anomalous absorption paradox." Each of these hypotheses has a somewhat different ramification for the spectral distribution of the excess absorption between the visible and near-infrared portions of the solar spectrum and, as such, cannot be resolved using standard broadband pyranometer measurements. For example, Twomey (1972, 1977) suggested that absorbing aerosol particles, either within the cloud droplets or interstitial to them, may be partly responsible for this excess absorption. Calculations by Newiger and Bähnke (1981) show that absorbing aerosol particles interstitial to the cloud droplets can enhance cloud absorption to values up to 30% of the incident solar radiation, but that this effect is largely restricted to wavelengths $\lambda \leq 1.5$ μm. The possibility also exists that leakage of radiation through the sides of clouds might account for some of the large values of absorption implied by the measurements (Welch et al., 1980; Ackerman and Cox, 1981). Wiscombe et al.

(1984) suggested that significant concentrations of large, drizzle-sized droplets could contribute to larger absorption values than typically obtained from calculations, but this effect would be restricted largely to wavelengths $\lambda \gtrsim 1.5$ μm. Finally, Stephens and Tsay (1990) suggested that an unobserved water-vapor continuum, if found to be present, might contribute to explaining this "anomalous absorption paradox."

In response to the widely recognized limitation of single-aircraft broadband pyranometer measurements, together with the need to spectrally resolve the absorption measurements in order to distinguish between the various competing anomalous absorption hypotheses, we were prompted to develop the diffusion domain method for determining the absorption of solar radiation by clouds as a function of wavelength (King, 1981). In this method, the intensity of scattered radiation deep within a cloud layer is measured as a function of zenith angle for selected wavelengths in the visible and near-infrared.

Figure 1 is a schematic illustration of the various regimes of an optically thick cloud layer illuminated from above by solar radiation incident at solar zenith angle θ_0. Deep within an optically thick medium, located sufficiently far from the top and bottom boundaries of the medium (cloud), the diffuse radiation field assumes an asymptotic form characterized by rather simple properties. In this region, known as the diffusion domain, the role of direct (unscattered) radiation is negligible compared to the role of diffuse radiation, the diffuse intensity field is azimuthally independent, and the relative angular distribution is independent of solar zenith angle. For a vertically homogeneous cloud layer at a wavelength for which the single scattering albedo $\omega_0 < 1$, the intensity in the diffusion domain is given by

$$I(\tau, u) = s_1 P(u) e^{-k\tau} + s_2 P(-u) e^{-k(\tau_c - \tau)} \tag{1}$$

where τ is the optical depth measured from the upper boundary of the cloud; τ_c is the total optical thickness of the cloud layer; u is the cosine of the zenith angle with respect to the positive τ direction ($-1 \leq u \leq 1$); $P(u)$ is the diffusion pattern (eigenfunction); k is the diffusion exponent (eigenvalue); and s_1 and s_2 are the strengths of the diffusion streams in the positive and negative τ directions, respectively (see Fig. 1). As the relative strengths between s_1 and s_2 depend only on τ_c and the optical properties of the cloud layer, the relative angular distribution of the diffuse radiation field is independent of solar zenith angle.

The transition between the upper- and lowermost levels of the cloud layer and the innermost diffusion domain occurs at a scaled optical depth $(1 - g)\tau \simeq 2$ from both the top and bottom boundaries of the cloud, where g is the asymmetry factor. This transition is shown schematically in Fig. 1 and numerically in Herman et al. (1980), but it is only approximate in that the transition is a gradual one and the precise level of the transition depends on the accuracy required of the asymptotic formulas applicable in the diffusion regime.

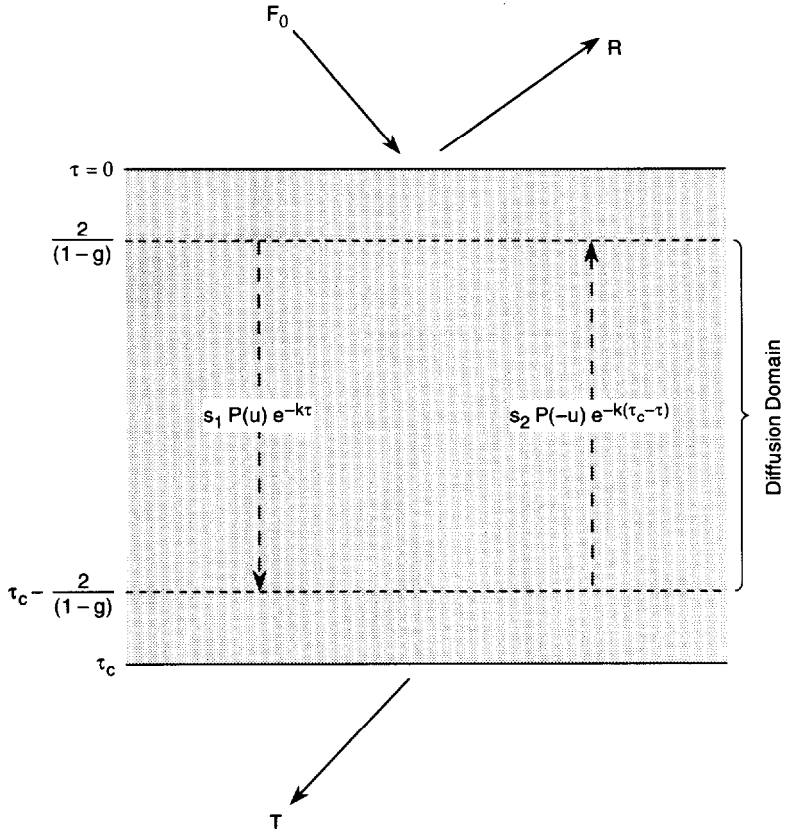

Figure 1 Schematic illustration of the radiation regimes of an optically thick, nonconservative cloud layer illuminated from above by solar radiation incident at a solar zenith angle θ_0. The diffusion domain, located deep within the cloud and sufficiently far from its top and bottom boundaries, is a regime characterized by azimuthally symmetric radiation that can be characterized by a sum of upward- and downward-propagating diffusion streams.

Figure 2 illustrates the relative intensity as a function of zenith angle for various values of the similarity parameter (s), where s is a function of the cloud asymmetry factor (g) and single scattering albedo (ω_0) as follows:

$$s = \left(\frac{1 - \omega_0}{1 - \omega_0 g} \right)^{1/2} \tag{2}$$

The zenith angle is here defined with respect to the downward-directed normal such that $\theta = 0°$ (180°) corresponds to a zenith (nadir) measurement or, alternatively, to nadir (zenith) propagating radiation. This figure pertains to computations

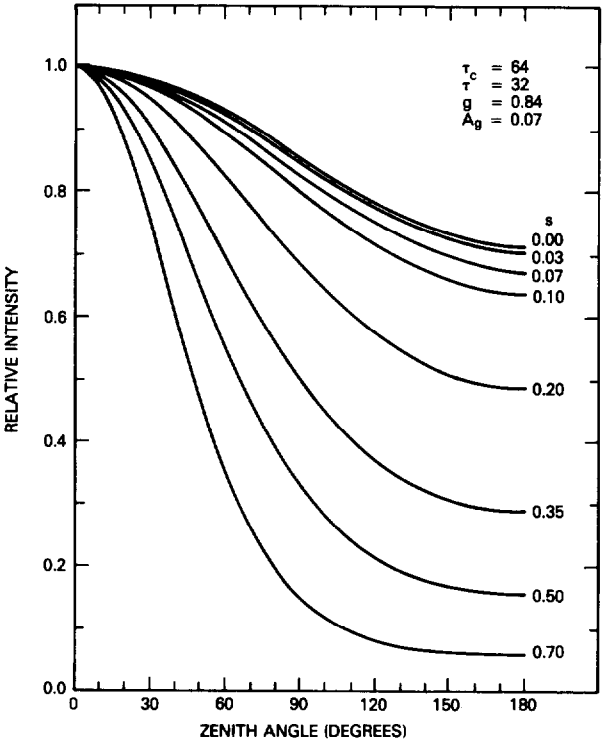

Figure 2 Relative intensity as a function of zenith angle and similarity parameter at the midlevel of a cloud of total optical thickness $\tau_c = 64$. These curves apply to a Henyey-Greenstein phase function with $g = 0.84$ and when the surface reflectance $A_g = 0.07$. (From King et al., 1986.)

made for an optical depth $\tau = 32$ in a cloud of total optical thickness $\tau_c = 64$ when the surface reflectance $A_g = 0.07$. These calculations, based on the phase function introduced by Henyey and Greenstein (1941) for $g = 0.84$, clearly show that the diffuse intensity field in the diffusion domain of an optically thick cloud layer is expected to monotonically decrease from zenith to nadir. Figure 2 shows computations of the internal scattered radiation field for similarity parameters ranging between 0.0 and 0.7 which, for an asymmetry factor $g = 0.84$, corresponds to $0.87 \leq \omega_0 \leq 1.0$.

Mel'nikova (1978) was the first to suggest that the ratio of the upward to downward propagating fluxes within the diffusion domain be used to determine the single scattering albedo of clouds. King (1981) demonstrated that the ratio of the nadir-to-zenith intensities within a cloud layer is far more sensitive to single scattering albedo than is the ratio of the upward-to-downward propagating fluxes, and further showed analytically that this ratio is a function solely of A_g, s, and the

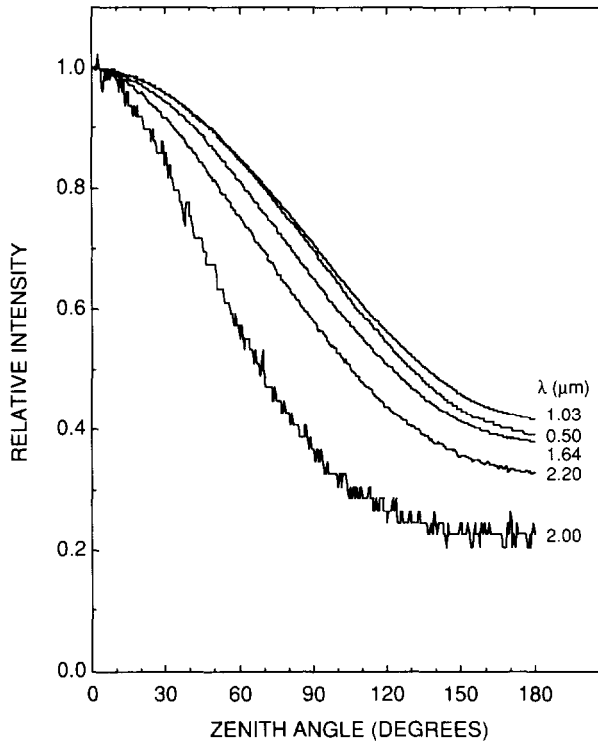

Figure 3 Relative intensity as a function of zenith angle and wavelength for internal scattered radiation measurements obtained with the cloud absorption radiometer on 10 July 1987. (From King et al., 1990.)

scaled optical depth between the aircraft flight level and the base of the cloud $[(1 - g)(\tau_c - \tau)]$.

The first experimental observations of the angular distribution of scattered radiation deep within a cloud layer, together with an analysis of the spectral similarity parameter derived from these measurements, were presented and discussed by King et al. (1990). The data were obtained using the cloud absorption radiometer (CAR) described by King et al. (1986), which flew on the University of Washington's Convair C-131A aircraft during the FIRE marine stratocumulus IFO, conducted off the coast of San Diego, California during July 1987. The microphysical structure of the clouds, including the cloud droplet size distribution, was also monitored continuously with instruments aboard the aircraft.

Figure 3 shows the relative intensity as a function of zenith angle obtained from measurements inside clouds for selected wavelengths of the cloud absorption radiometer. Aside from the quantization (digitization) noise in the shortest wave-

length channels and instrumental (electrical) noise in the longest wavelength channels, two main features can be seen on examination of Fig. 3. These are (1) the angular intensity field at the shortest wavelength follows very nearly the cosine function expected for conservative scattering in the diffusion domain, and (2) the angular intensity field becomes increasingly anisotropic as absorption increases. This is especially noticeable at 2.0 μm, the instrument channel where water droplets have their greatest absorption. The experimental observations presented in Fig. 3 complement the theoretical figure (for selected values of the similarity parameter rather than wavelength) presented in Fig. 2.

Finally, making use of the analytic formulations inherent in the diffusion domain method, together with measurements obtained with the cloud absorption radiometer, King et al. (1990) derived the spectral similarity parameter for clouds in a 50-km section of marine stratocumulus located some 355 km southwest of the airfield on Coronado Island, San Diego. These results, presented in Fig. 4, illustrate the mean and standard deviation of the spectral similarity parameter for all 13 channels of the CAR obtained on 10 July 1987. Although the conversion

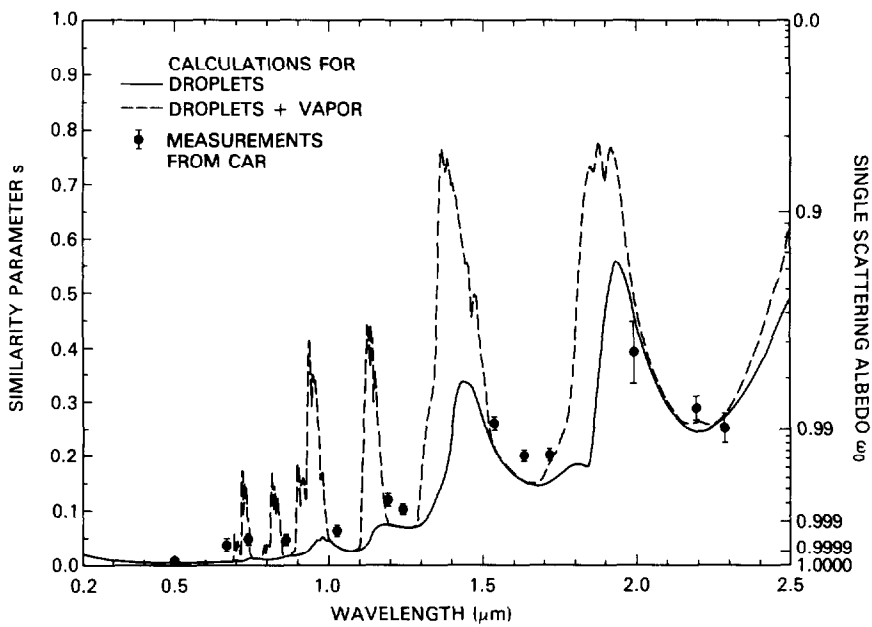

Figure 4 Calculations of the similarity parameter s as a function of wavelength for water droplets alone (solid line) and drops plus vapor (dashed line) for the cloud droplet size distribution and water vapor conditions of the marine stratocumulus cloud of 10 July 1987. The single scattering albedo scale is valid at $\lambda = 0.754$ μm, where the cloud asymmetry factor $g = 0.848$. The measurements derived from the cloud absorption radiometer (solid circles with error bars) are averages of the similarity parameter derived by applying the diffusion domain method to a 50-km section of this cloud. (From King et al., 1990.)

from s to ω_0 is not unique, due to the moderate spectral variation of g, a single scattering albedo scale has been provided in this figure as a matter of convenience. This scale, shown on the right-hand side of Fig. 4, is strictly applicable at $\lambda = 0.754$ μm. Based on profile ascents and descents following these measurements, the stratocumulus cloud layer was determined to be 440 m thick with a cloud base at approximately 490 m.

In addition to the experimental results obtained using the CAR, Fig. 4 illustrates calculations of the similarity parameter as a function of wavelength for a cloud composed of water droplets only (solid curve) and droplets plus saturated vapor at 10.3°C (dashed curve). The water droplet computations were based on calculations for the measured cloud droplet size distribution. The water-vapor computations, on the other hand, were based on assuming the cloud was composed of saturated vapor having a column loading of water vapor of 0.45 g cm^{-2}. The water-vapor transmission functions were computed for this cloud layer at a resolution of 20 cm^{-1} using LOWTRAN 5 (Kneizys et al., 1980). The absorption optical depths thus obtained were combined with the corresponding optical properties for cloud droplets, where the total optical thickness of the cloud was assumed to be 16 at a wavelength of 0.754 μm. The total optical thickness of this 50-km section of cloud was approximately 32.3 ± 4.2, which affects the relative weighting between cloud droplets and water vapor. We recalculated the theoretical curves in Fig. 4 using LOWTRAN 7 (Kneizys et al., 1988) and $\tau_c = 16$ and 32, but these differences have only a minor impact on the conclusions drawn from this figure.

The results presented in Fig. 4 show that, *in this case*, the measured absorption of solar radiation by clouds is close to, but persistently larger than, theoretical calculations. Furthermore, these findings support the view that clouds absorb more and reflect less solar radiation than theoretical predictions. It was not possible to bring theory and measurements into complete agreement by simply postulating an error in the measurement of the effective radius (r_e), as this would improve the agreement in some parts of the spectrum and worsen the agreement in other parts of the spectrum.

The close agreement between measurements and theory in this case, where measurements show a small but consistently larger absorption than theoretical predictions, is consistent with modest "anomalous absorption" in these clouds that were largely free of anthropogenic influence. The single scattering albedos that we obtained from our analysis in the visible wavelength region, though somewhat lower than theory, are still ~0.9999, values generally much too large to explain any reduced reflection by these clouds ($20 \lesssim \tau_c \lesssim 42$). On the other hand, in the wavelength region between 1.6 and 2.2 μm, our measurements of excess absorption are consistent with the observations of Twomey and Cocks (1982), Stephens and Platt (1987), and Foot (1988), who reported unusually low spectral reflectance in this wavelength region. Furthermore, recent changes in computations of water vapor absorption properties within both the absorption bands and

window regions of the near-infrared, as reflected in LOWTRAN 7 (Kneizys et al., 1988), suggest that the theoretical calculations in the presence of water vapor (dashed line in Fig. 4) may have to be modified to some degree. Thus, it appears that a combination of new measurement techniques, new instruments, and revisions in our theoretical treatment of water vapor absorption in light of new measurements of line parameters are all promising new advances that are leading toward a solution of this four-decade-old anomaly in the shortwave absorption by terrestrial water clouds.

B. Cloud Optical Thickness and Effective Particle Radius

A number of efforts have been devoted to determining the cloud optical thickness and/or effective particle radius from reflected solar radiation measurements, both from aircraft (Hansen and Pollack, 1970; Twomey and Cocks, 1982, 1989; King, 1987; Foot, 1988; Rawlins and Foot, 1990; Nakajima et al., 1991) and satellite (Curran and Wu, 1982; Arking and Childs, 1985; Rossow et al., 1989) platforms. In each of these methods, multiwavelength radiometers have been used to obtain measurements of the reflection function $R(\tau_c;\ \mu,\ \mu_0,\ \phi)$, formed from a ratio of the reflected intensity $I(0,\ -\mu,\ \phi)$ and the incident solar flux F_0 as follows:

$$R(\tau_c;\ \mu,\ \mu_0,\ \phi) = \frac{\pi I(0,\ -\mu,\ \phi)}{\mu_0 F_0} \tag{3}$$

In this expression μ_0 is the cosine of the solar zenith angle θ_0; μ is the absolute value of the cosine of the zenith angle θ, measured with respect to the positive τ direction; and ϕ is the relative azimuth angle between the direction of propagation of the emerging radiation and the incident solar direction.

Radiative transfer theory shows that the reflection function of optically thick layers is largely a function of the scaled optical thickness $\tau_c' = (1 - \omega_0 g)\tau_c$ and the similarity parameter s, where the similarity parameter, in turn, depends primarily on the effective particle radius, defined by (Hansen and Travis, 1974)

$$r_e = \int_0^\infty r^3 n(r)\ dr \ / \ \int_0^\infty r^2 n(r)\ dr \tag{4}$$

where $n(r)$ is the particle size distribution and r is the particle radius. In addition to τ_c', s, and A_g, the details of the single scattering phase function affect the directional reflectance of the cloud layer (King, 1987).

The fundamental principle behind the simultaneous determination of the cloud optical thickness and effective particle radius is that the reflection function of clouds at a weakly absorbing channel in the visible wavelength region is primarily a function of the cloud optical thickness, whereas the reflection function at a water (or ice) absorbing channel in the near-infrared is primarily a function of cloud particle size. This can most easily be seen on examination of Fig. 5, which shows simultaneous computations of the reflection function of clouds at 0.75 and

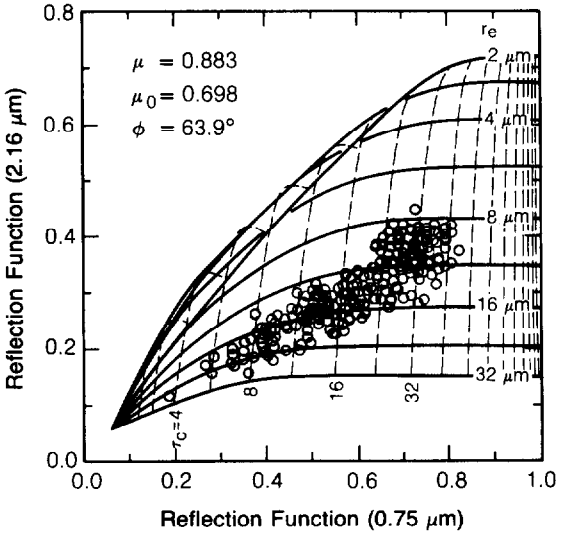

Figure 5 Theoretical relationship between the reflection function at 0.75 and 2.16 μm for various values of the cloud optical thickness (at $\lambda = 0.75$ μm) and effective particle radius for the case when $\theta_0 = 45.7°$, $\theta = 28.0°$, and $\phi = 63.9°$. Data from measurements above marine stratocumulus clouds during FIRE are superimposed on the figure. (From Nakajima and King, 1990.)

2.16 μm for various values of τ_c and r_e when $\theta_0 = 45.7°$, $\theta = 28.0°$, and $\phi = 63.9°$. These angles correspond to a case for which observations were obtained of the reflectance of marine stratocumulus clouds during FIRE in July 1987. The data points superimposed on this figure were obtained from the NASA ER-2 aircraft using the multispectral cloud radiometer (MCR) described by Curran et al. (1981) and King (1987), from which we conclude that this 145-km section of cloud had an optical thickness at 0.75 μm that ranged between 6 and 45 with an effective radius that ranged between 8 and 22 μm.

Whether one formulates the retrieval of r_e in terms of a ratio of the reflection function at two wavelengths, as in Foot (1988), Twomey and Cocks (1989), and Rawlins and Foot (1990), or as an absolute reflection function, as in Curran and Wu (1982) and Nakajima and King (1990), the underlying physical principles behind the retrieval remain the same. As the effective radius increases, absorption monotonically increases for all $r_e \gtrsim 1$ μm. As a consequence, cloud reflectance in the near-infrared (e.g., 2.16 μm) generally decreases (see Fig. 5). At a weakly absorbing channel in the visible wavelength region (e.g., 0.75 μm), on the other hand, the reflection function depends primarily on the total optical thickness such that τ_c increases as the the reflection function increases.

During the marine stratocumulus IFO, a major effort was expended in obtaining data sets of both the spectral reflection and microphysical properties of clouds to enable these remote sensing concepts to be validated. Figure 6 compares the

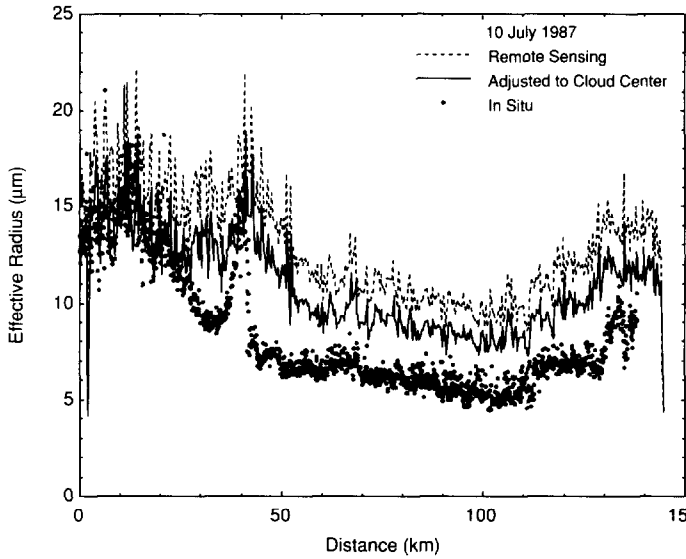

Figure 6 Comparison of the effective radius as a function of distance along the nadir track of the ER-2 aircraft derived from remote sensing (dashed line) and *in situ* measurements from the C-131A aircraft (solid circles). The solid line represents the expected values of effective radius at the geometric center of the cloud layer, derived from the remote-sensing measurements by allowing for vertical inhomogeneity of droplet radius. (From Nakajima et al., 1991.)

retrieved effective radius with *in situ* estimates obtained along the nadir track of the ER-2 aircraft. The remote sensing values of the effective radius (dashed curve) were adjusted to the expected values at the geometric center of the cloud layer (solid curve) using the method outlined by Nakajima and King (1990), thereby taking into account the vertical distribution of microphysical properties typical of marine stratocumulus clouds. This case study (after Nakajima et al., 1991) is unique in that the ER-2 aircraft was well coordinated with the University of Washington C-131A aircraft, which was making nearly simultaneous *in situ* microphysical measurements (solid circles). These results clearly show that the shape of the retrieved r_e time series is generally similar to, but systematically larger than, the direct *in situ* measurements of the effective radius. These results suggest, therefore, that clouds reflect less solar radiation at 2.16 μm than theoretically predicted (see Fig. 5), which is likewise consistent with cloud absorption being enhanced over theory in this "window" region (see Fig. 4).

A similar conclusion was reached by Twomey and Cocks (1989), who measured the spectral reflectance of marine stratus off the coast of eastern South Australia and subsequently measured the droplet size distribution from the same aircraft platform. Figure 7 is a histogram of the effective radius derived from their five-channel remote sensing algorithm and from *in situ* microphysical measurements. One again draws the conclusion that remote sensing overestimates the ef-

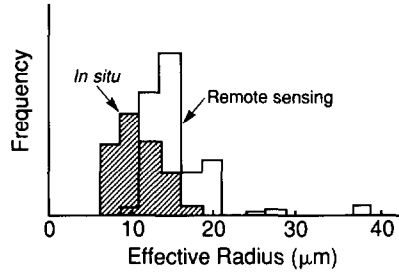

Figure 7 Histogram plot of the frequency distribution of inferred effective radius for one day's observations as derived by remote sensing (open histogram) and as derived from *in situ* microphysical measurements (hatched). (From Twomey and Cocks, 1989.)

fective radius in comparison with *in situ* measurements. To clarify the bias in the retrieved values of r_e, Twomey and Cocks (1989) presented cumulative distributions of r_e derived from both remote sensing and *in situ* measurements. These results, presented in Figs. 8a (logarithmic scale) and 8b (linear scale), clearly show that remote sensing overestimated the effective radius by ~5 μm (~40%), and was more like an offset (bias) than a percentage overestimation (similar to the conclusions of Nakajima et al., 1991).

Rawlins and Foot (1990) utilized the United Kingdom C-130 aircraft during the FIRE marine stratocumulus experiment to determine τ_c and r_e from remote sensing measurements. They utilized both reflection and transmission function measurements, and in both cases found their retrieved values of r_e to be in excess of *in situ* microphysical measurements by some 2–3 μm (25–50%). In addition, Rawlins and Foot (1990) obtained better agreement in r_e for the optically thinner parts of the cloud, as did Nakajima et al. (1991). This is contrary to expectations, in that one would expect a retrieval algorithm based on spectral reflectance mea-

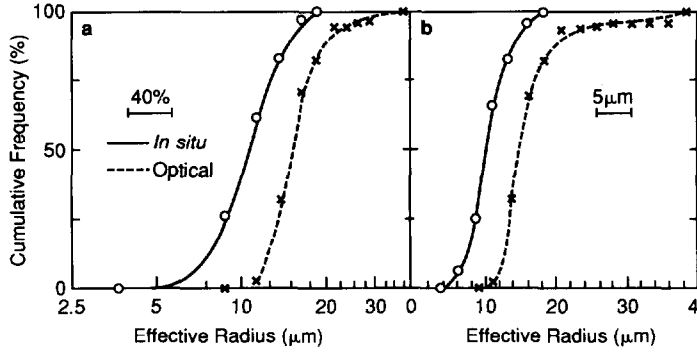

Figure 8 Cumulative distribution of remotely sensed and *in situ* values of effective radius plotted on (a) a logarithmic scale, and (b) a linear scale. (From Twomey and Cocks, 1989.)

surements to be more accurate for optically thick clouds due to the enhanced sensitivity to absorption arising from increased multiple scattering. Both Rawlins and Foot (1990) and Nakajima et al. (1991) obtained satisfactory estimates of the cloud optical thickness (not shown), further suggesting that the bulk of the discrepancy in the retrieval of τ_c and r_e is largely confined to the optical properties of clouds in the near-infrared (e.g., 2.16 μm).

Although some discrepancy still remains between *in situ* and remote sensing estimates of r_e, the bulk of recent evidence suggests that the excess absorption by clouds is largely restricted to the water-vapor window regions of the near-infrared. Numerous studies have demonstrated that clouds absorb more and reflect less solar radiation than theoretically predicted. Stephens and Tsay (1989) were the first to suggest that an overlooked absorption by water vapor in these window regions could explain many of the observed discrepancies. In fact, Rawlins and Foot (1990), Nakajima et al. (1991), and, we suspect, Twomey and Cocks (1989), all used LOWTRAN 5 (Kneizys et al., 1980) to provide the water vapor absorption coefficients used in their retrieval schemes. LOWTRAN 7 (Kneizys et al., 1988) differs substantially from LOWTRAN 5 in its water vapor continuum and absorption line parameters, as well as in its pressure and temperature scaling for inhomogeneous vertical paths. Recently Taylor (1992) reanalyzed many of the data sets previously reported by Rawlins and Foot (1990), this time using LOWTRAN 7. He found that the bias in the retrieved values of r_e that Rawlins and Foot (1990) found when they used LOWTRAN 5 largely disappeared when the water vapor transmission characteristics of LOWTRAN 7 were used. In addition, Nakajima et al. (1991) demonstrated that their biases in r_e were the most consistent with excess absorption by water vapor in the near-infrared and were completely inconsistent with excess absorption within the cloud droplets or interstitial to the droplets.

In spite of the discrepancy that still remains between *in situ* and remote sensing estimates of r_e, it is nevertheless intriguing to examine the joint probability density function of τ_c and r_e for marine stratocumulus clouds, especially given the recent interest in parameterizing the shortwave radiative properties of clouds in terms of liquid water path (W) and effective radius (Slingo, 1989). Figure 9a shows joint probability density functions of τ_c and r_e derived from MCR images on each of four days during FIRE (after Nakajima et al., 1991), where each probability density function was derived from an image 35 km in width and 105–165 km in length, depending on the day. The contour lines for each day correspond to the 10, 30, 50, 70, and 90% occurrence levels, from which the mode and interquartile ranges can readily be inferred. Comparable results for W and r_e are presented in Fig. 9b, where the cloud optical thickness was converted to liquid water path using the relation (Stephens, 1978)

$$W = \frac{2\rho}{3} \tau_c r_e \tag{5}$$

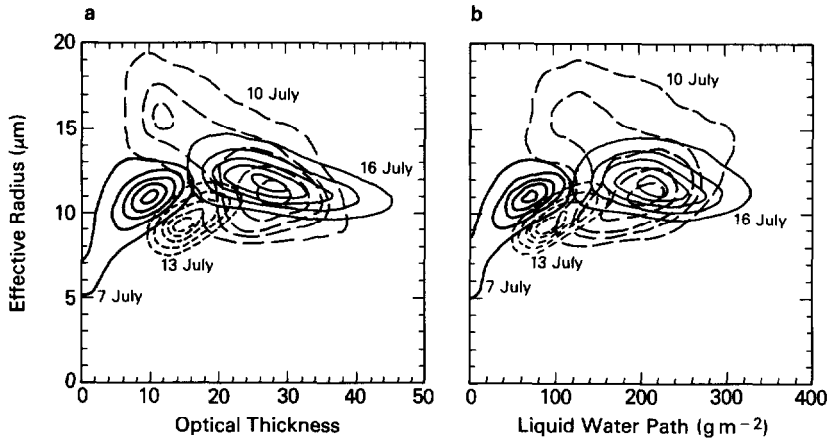

Figure 9 Joint probability density functions of (a) the cloud optical thickness and effective radius, and (b) the liquid water path and effective radius, for four days during FIRE. These results were derived from MCR measurements acquired from the ER-2 aircraft, where the effective radius r_{remote} has not been adjusted to the geometric center of the cloud layer. The five contour lines for each day correspond to the 10, 30, 50, 70, and 90% occurrence levels. (From Nakajima et al., 1991.)

where W is the liquid water path (g m^{-2}), ρ is the density of water (g cm^{-3}), and r_e is the effective radius (μm).

Figure 9 shows a distinct positive correlation between τ_c (or W) and r_e on the optically thin days of 7 and 13 July, and a modest negative correlation on the optically thick days of 10 and 16 July. Statistical properties like those presented in Fig. 9 are extremely important for climate studies, not simply because the joint retrieval of τ_c and r_e seems possible, but because the shortwave radiative properties of water clouds depend almost exclusively on these two parameters (Slingo, 1989).

C. Variability of Spectral Reflectance

On two different days during the FIRE marine stratocumulus experiment, the University of Washington C-131A and United Kingdom C-130 aircraft flew tightly coordinated flight tracks above, within, and below clouds. Figure 10 shows an intercomparison of the reflected intensity obtained on one such occasion (5 July 1987) when both aircraft were flying wingtip to wingtip for calibration intercomparison purposes. Each aircraft observed the reflected intensity in the nadir direction using its respective narrow field-of-view radiometer: the scanning cloud absorption radiometer with its 13 visible and near-infrared channels in the case of the C-131A (King et al., 1986), and the nadir-viewing multichannel radiometer with its eight visible and near-infrared channels in the case of the C-130 (Foot,

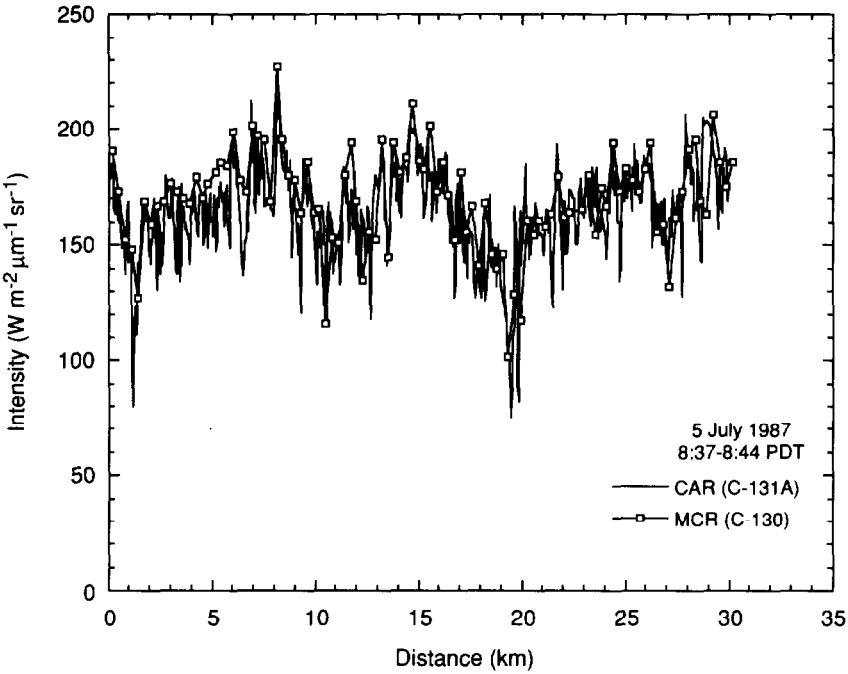

Figure 10 Comparison of the reflected intensity as a function of distance along the flight track of University of Washington C-131A and United Kingdom C-130 aircraft. These data were obtained above marine stratocumulus clouds on 5 July 1987 using the cloud absorption radiometer at 0.5 μm (solid line) and the multichannel radiometer at 0.55 μm (open squares).

1988; Rawlins and Foot, 1990). Figure 10 clearly shows that the visible calibration was quite similar for both radiometers on this day, and further that the reflected intensity of these marine stratocumulus clouds exhibited a cellular spatial structure. On this day the reflectance of the clouds varied with a wavelength of approximately 10 km, even though the clouds were geometrically quite flat on top. We attribute these reflectance variations to variations in the optical thickness (liquid water path) and, to a lesser extent, effective radius. We would further like to emphasize that these clouds, although generally flat on top, often exhibited variations in the cloud base, necessarily leading to variations in the geometric thickness of the clouds.

D. Angular Transmission Characteristics

In addition to angular and spectral reflectance measurements and internal scattered radiation measurements, information on the radiative properties of clouds can be

determined from the angular distribution of transmitted radiation beneath an optically thick cloud layer. This was shown by Rawlins and Foot (1990), who utilized zenith measurements of transmitted radiation beneath clouds to determine τ_c and r_e. They found that transmission measurements, although far less sensitive to microphysical properties than reflectance measurements, yield estimates of the effective radius that are entirely consistent with near-infrared reflectance measurements. The self-consistency of their reflection and transmission-derived values of r_e negates the possibility that their retrieval bias, discussed in Section II.B, could have arisen from a calibration error. This is because any calibration adjustment required to bring the spectral reflectance estimates into agreement with *in situ* measurements would necessarily lead to accentuating the bias errors resulting from the transmission measurements.

A further example of the use of transmission measurements can be found in Fig. 11, which shows the intensity as a function of zenith angle for $\lambda = 0.673$ μm and a single scan of the cloud absorption radiometer beneath a marine stratocumulus cloud layer on 13 July 1987. The angular distribution of the transmitted radiation beneath the cloud layer is seen to monotonically decrease from zenith to horizon, in close accord with our expectations for optically thick cloud layers in which the transmitted intensity $I(\tau_c; \mu, \phi)$ for conservative scattering is expected to be azimuthally independent and to follow the functional form (King, 1987)

$$I(\tau_c; \mu, \phi) = \frac{4\mu_0 F_0 K(\mu_0)[(1 - A_g)K(\mu) + A_g]}{\pi[3(1 - A_g)(1 - g)(\tau_c + 2q_0) + 4A_g]} \tag{6}$$

In this expression q_0 is the extrapolation length, representing a virtual optical depth beneath the cloud layer from which the transmitted solar radiation is reflected back up to the cloud, $q' = (1 - g)q_0$ is the reduced extrapolation length ($\simeq 0.714$), $K(\mu)$ is the escape function, and all other constants have previously been defined. From this expression, it follows that the transmitted intensity beneath an optically thick cloud layer ($\tau_c \gg 2q_0 \simeq 9.4$) overlying a low-reflectance surface (such as the ocean) is given approximately by

$$I(\tau_c; \mu, \phi) \propto \frac{K(\mu)}{(1 - g)\tau_c} \tag{7}$$

Thus, it follows that an angular transmission measurement, such as the one shown in Fig. 11, in conjunction with a theoretical calculation of the escape function (King, 1987), can easily be used to determine the optical thickness of a cloud layer. For an optically thick cloud, such as the one from which the measurements in Fig. 11 were obtained, the transmitted intensity is inversely proportional to the scaled optical thickness $(1 - g)\tau_c$. The low reflectance for $\theta \geq 90°$ corresponds to reflectance by the ocean surface.

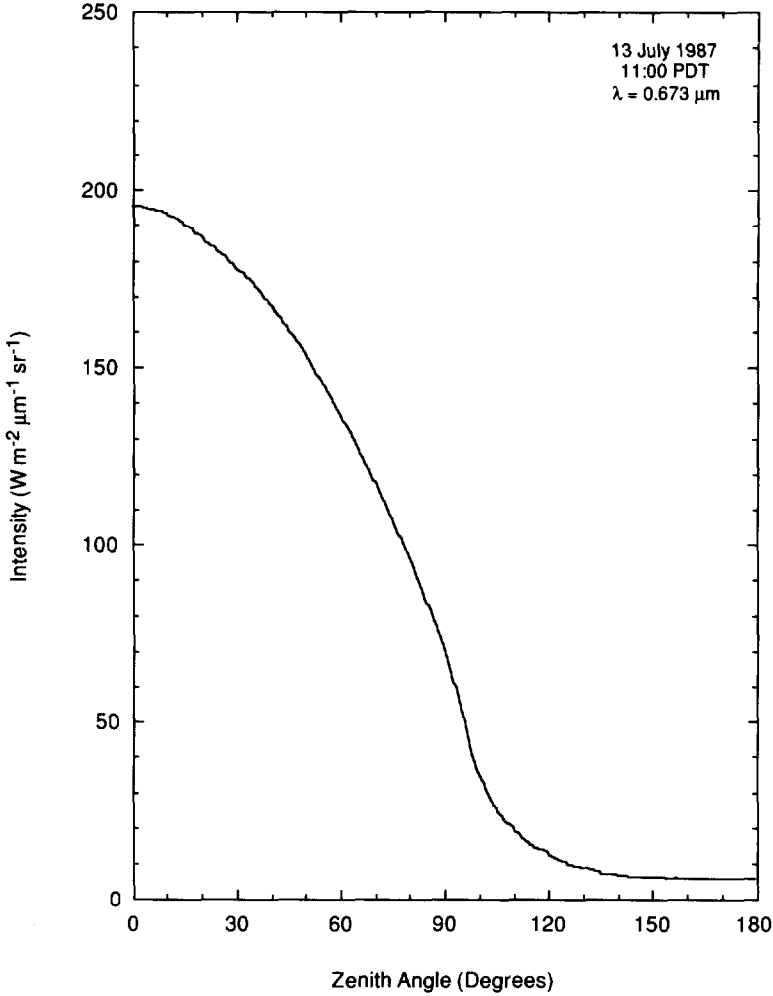

Figure 11 Intensity as a function of zenith angle for measurements obtained with the cloud absorption radiometer beneath clouds at $\lambda = 0.673$ μm. This scan applies to measurements taken over the ocean on 13 July 1987.

III. Cirrus Clouds

Cirrus clouds were the focus of intensive field observations in the United States in 1986 (Starr, 1987) and 1991 (FIRE II cirrus IFO), and in Europe in 1989 (International Cirrus Experiment). These clouds, like marine stratocumulus clouds, are sensitive regulators of the earth's climate (Ramanathan et al., 1983, 1989) and are difficult to sense from remote satellite platforms. In the case of optically thin cirrus

clouds, they often have little effect on reflected solar radiation but have a significant influence on the infrared radiative properties of the earth–atmosphere–ocean system. In the following sections we will describe some of the key findings on the radiative properties of cirrus clouds deduced from aircraft observations during the FIRE cirrus IFO, conducted in south-central Wisconsin during October and November 1986.

A. Thermal Emission Characteristics

Figure 12 shows measurements of the brightness temperature spectrum observed between 600 and 1100 cm^{-1} (9.1 and 16.7 μm) using the nadir-viewing high-resolution interferometer sounder (HIS) flown on the ER-2 aircraft during 2 November 1986. Major absorption bands in the earth's atmosphere are evident in this figure as lower temperatures, representing emission from layers of the atmosphere up to 70 K colder than the earth's surface. The dominant absorption bands in this figure are the 15-μm CO_2 band ($580 \lesssim \nu \lesssim 760\ cm^{-1}$) and the 9.6-$\mu m$ O_3 band ($1000 \lesssim \nu \lesssim 1070\ cm^{-1}$). The four curves presented in this figure represent measurements of upwelling (zenith propagating) thermal radiation from clear scenes

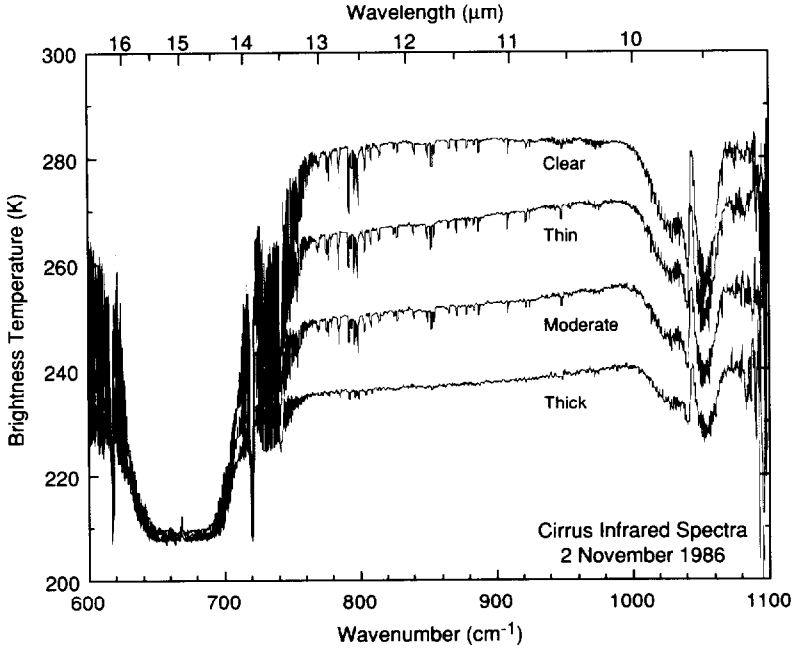

Figure 12 HIS brightness temperature spectra obtained between 600 and 1100 cm^{-1} (9.1 and 16.7 μm) over clear scenes and optically thin, moderate, and thick cirrus clouds during the FIRE cirrus experiment. (From King et al., 1992.)

and optically thin, moderate, and thick cirrus clouds. Over the clear land scene, the thermal emission in the 11-μm window region is spectrally quite flat, suggesting that the emissivity of the land surface is nearly the same at 11 and 12 μm (i.e., $\epsilon_{11} \simeq \epsilon_{12} \simeq 1.0$). In contrast, cirrus clouds tend to emit radiation with a higher brightness temperature at 11 μm than at 12 μm. This is because the emissivity of these optically thin ice clouds varies with wavelength and is everywhere less than unity ($\epsilon_{12} \geq \epsilon_{11}$). As the optical thickness increases and the emissivity of the clouds approaches unity, the brightness temperature difference once again disappears, as in the case of clear skies. In this case, however, the temperature of the scene is colder, corresponding to the temperature at the tops of the clouds. This principle, discussed in detail by Wu (1987) and Prabhakara et al. (1988), necessarily leads to the "droop" in the brightness temperature ($T_{11} - T_{12}$) observed in these measurements. Further examples of infrared emission spectra of cirrus clouds obtained from the Nimbus 4 interferometer spectrometer (IRIS) can be found in Prabhakara et al. (1990).

B. Effective Radius of Ice Crystals

Prabhakara et al. (1988) were among the first to demonstrate the sensitivity of the brightness temperature difference ($T_{11} - T_{12}$) to effective particle radius and infrared optical thickness of cirrus clouds. Figure 13 shows calculations of the brightness temperature difference ($T_{10.8} - T_{12.6}$) as a function of the brightness temperature at 10.8 μm ($T_{10.8}$) for various values of the effective radius and infrared optical thickness. These calculations, based on a tropical atmosphere with 4 g cm^{-2} of precipitable water in which there are spherical ice crystals in a 1 km thick cloud near 9 km altitude (240 K) overlying an ocean with a sea-surface temperature of 300 K, show that the brightness temperature difference is everywhere positive. Furthermore, the temperature difference tends to be small for clear skies ($\tau_c = 0$, $T_{10.8} = 293$ K) and for optically thick clouds ($\tau_c \gtrsim 4$, $T_{10.8} \simeq 240$ K), with the greatest brightness temperature difference associated with small ice crystals and $\tau_c \simeq 1$, where the optical thickness here refers to the optical thickness at 10.8 μm.

Prabhakara et al. (1988) determined the global distribution of this brightness temperature difference from Nimbus 4 IRIS observations, and concluded that seasonal mean differences in excess of 8 K were frequently encountered in the tropical oceans, especially in the warm pool region of the western Pacific. They attribute these differences to the high frequency of optically thin cirrus clouds composed of small ice crystals. In addition to these satellite observations, Ackerman et al. (1990) examined the infrared radiative properties of cirrus clouds using HIS observations from the ER-2 aircraft during the FIRE cirrus IFO. They noted that the 8.55 μm window region is centered on a region containing weak water-vapor absorption lines, whereas 11 and 12 μm are in windows largely unaffected by water-vapor absorption lines. They further showed that the brightness temper-

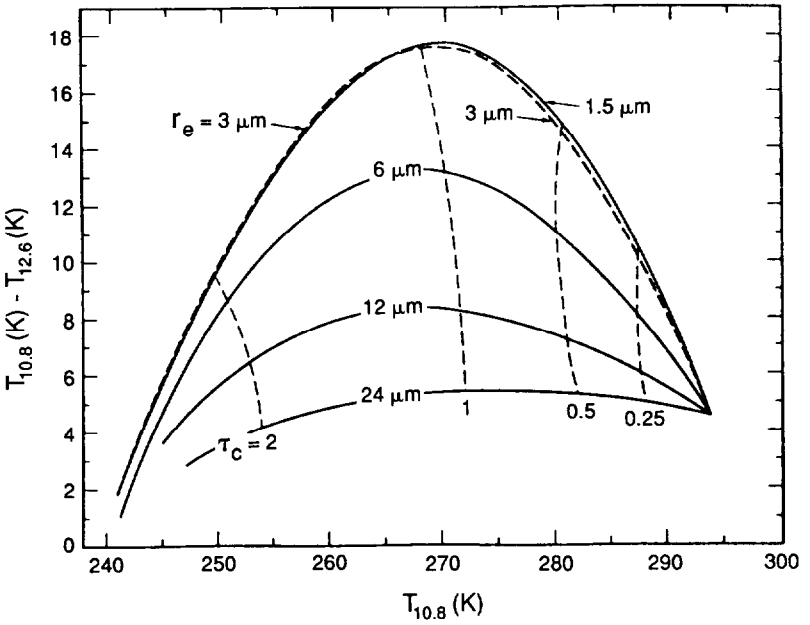

Figure 13 Theoretical brightness temperature difference between 10.8 and 12.6 μm as a function of the corresponding brightness temperature at 10.8 μm for high-level (cirrus) spherical ice crystal clouds as a function of effective radius and infrared optical thickness. (From Prabhakara et al., 1988.)

ature at 8.55 μm ($T_{8.5}$) generally exceeds that at 11 μm (T_{11}) over optically thin cirrus clouds, but it is less over clear sky regions. As a consequence, the brightness temperature difference $T_{8.5} - T_{11}$ is an even more sensitive indicator of optically thin cirrus clouds than is the brightness temperature difference $T_{11} - T_{12}$. Based on their observations during FIRE, they concluded that cirrus clouds are often composed of small ice crystals, with 8% of the cases having $10 \leq r_e < 30$ μm, 80% of the cases having $30 \leq r_e \leq 40$ μm, and 12% of the cases having $r_e > 40$ μm.

In addition to thermal emission measurements obtained with the nadir-viewing HIS, the ER-2 aircraft flown during the FIRE cirrus IFOs contained imaging radiometers and a monostatic Nd:YAG cloud and aerosol lidar system (Spinhirne et al., 1982, 1983). Plate 1, from Spinhirne and Hart (1990), shows a cross section of the lidar depolarization ratio as a function of distance as the aircraft flew over multilayer clouds on 28 October 1986, where the depolarization ratio δ is here defined as the ratio of the lidar return signal polarized perpendicular ($P_\perp$) to that polarized parallel ($P_\parallel$) to the transmitted laser pulse:

$$\delta = P_\perp / P_\parallel \tag{8}$$

The pulse repetition rate of the 0.532-μm laser was 5 Hz, resulting in a horizontal sampling interval of 40 m at the nominal aircraft speed of 200 m s^{-1}. This figure clearly shows that in the optically thin upper (cirrus) cloud the depolarization ratio typically ranged between 0.4 and 0.5, strongly suggesting the presence of nonspherical ice crystals. The lower (altocumulus) cloud layer, on the other hand, exhibited low values of the depolarization ratio ($\lesssim 0.05$ near cloud top at an altitude of ~7.4 km), indicative of backscattering from spherical water droplets. The presence of supercooled water droplets in the altocumulus clouds and nonspherical ice crystals in the cirrus clouds was confirmed from nearly coincident *in situ* microphysical measurements by Heymsfield et al. (1990). The vertical cloud streamer located between 7.2 and 7.5 km at a distance of ~180 km is apparently due to an aircraft contrail, perhaps that of the *in situ* King Air aircraft.

From scanning radiometer measurements on the ER-2 aircraft, Spinhirne and Hart (1990) determined the brightness temperature at 11.2 μm ($T_{11.2}$) and the brightness temperature difference $\Delta T = T_{11.2} - T_{12.4}$ as a function of flight track distance. These results, presented in Fig. 14, correspond to the same time interval and aircraft flight track as presented in Plate 1. These results show that when the scene beneath the aircraft consists exclusively of optically thin cirrus clouds, as between 30 and 100 km, the brightness temperature difference lies in the range

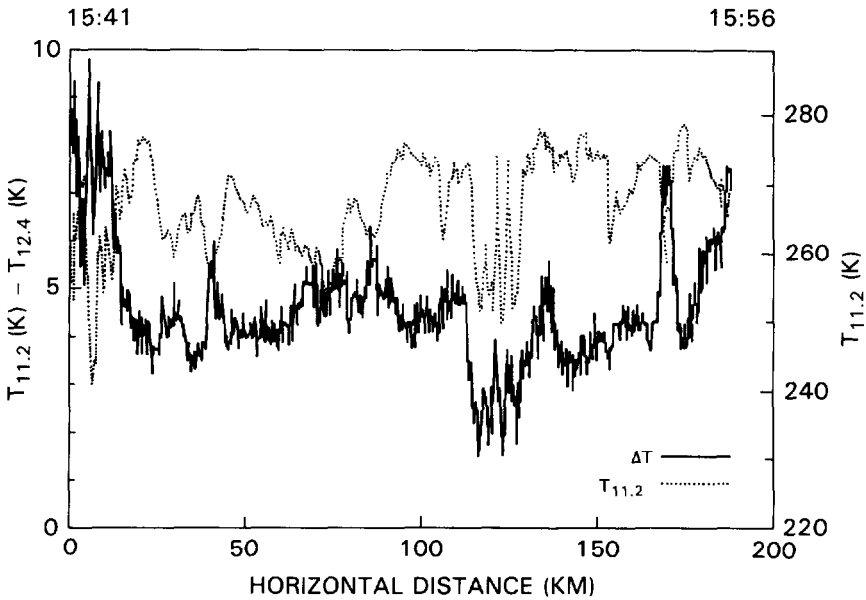

Figure 14 Brightness temperature at 11.2 μm and the brightness temperature difference $\Delta T = T_{11.2} - T_{12.4}$ as a function of flight track distance for nadir observations of cirrus clouds by the ER-2 on 28 October 1986. The brightness temperature difference varies with distance primarily as a result of the presence and optical characteristics of the lower cloud layer. (From Spinhirne and Hart, 1990.)

$4 \leq \Delta T \leq 5$ K. Calculations, such as the ones presented by Prabhakara et al. (1988) and shown in Fig. 13, therefore suggest that the upper-level cirrus cloud was composed of ice crystals having an effective radius in the range $12 \leq r_e \leq 24$ μm. In the portion of the scene containing cirrus clouds above optically thick altocumulus clouds, the brightness temperature difference ΔT is even larger than in the case of cirrus clouds alone. This is because these altocumulus clouds, found near the beginning and end of the flight line, are composed primarily of small water droplets. Had the lidar not been available to distinguish the multilayer nature of this cloud system, the infrared data alone would likely have been misinterpreted as suggesting the presence of quite small ice crystals. In the region between 120 and 130 km, where a lower-level cirrus cloud occurs in the absence of either an upper-level cirrus or lower-level altocumulus cloud, the brightness temperature difference is once again small, suggesting a region having relatively large ice crystals. In general, the cirrus cloud layer above 9 km was composed of the smallest ice crystals, those having $r_e \leq 25$ μm, and the lower-level cirrus cloud layer to ice crystals for which $r_e > 25$ μm.

Finally, Wielicki et al. (1990) used near-infrared reflectance measurements to estimate the effective radius of ice crystals in cirrus clouds using Landsat thematic mapper (TM) data obtained during the FIRE cirrus IFO. In general, they found that the satellite near-infrared reflection function measurements were largely consistent with values of $r_e \simeq 60$ μm, again far smaller than available *in situ* microphysical measurements ($r_e \simeq 200$ μm). All of these radiation measurements, taken together, suggest that the effective particle radius of ice crystals in the earth's atmosphere is much smaller than our current ability to measure it. This difficulty arises primarily from the fact that the principal cloud microphysics probes used today are based on light-scattering properties of spherical particles. Much effort needs to be expended in improving *in situ* particle-sizing capability, especially for the small ice particle sizes most often inferred from remote sensing of cirrus clouds.

C. Relationship between Thermal Emittance and Visible Albedo

The relationship between the thermal emission and shortwave reflection properties of cirrus clouds is important for assessing the radiative impact of cirrus clouds on the earth's climate (Arking, 1991). During the FIRE cirrus IFO Spinhirne and Hart (1990) measured the thermal emission at 10.84 μm and the reflection function at 0.75 μm using the narrow field of view MCR. Nadir observations of these parameters were obtained over cirrus clouds and clear sky conditions for the entire ER-2 flight track on 28 October 1986, a flight track that extended from central Wisconsin to overflights of Lake Michigan. After correcting this extensive data set for variable surface reflectance and further converting the nadir reflection function to plane albedo in accordance with the bidirectional reflectance model of Platt et al. (1980), Spinhirne and Hart (1990) were able to determine the relation-

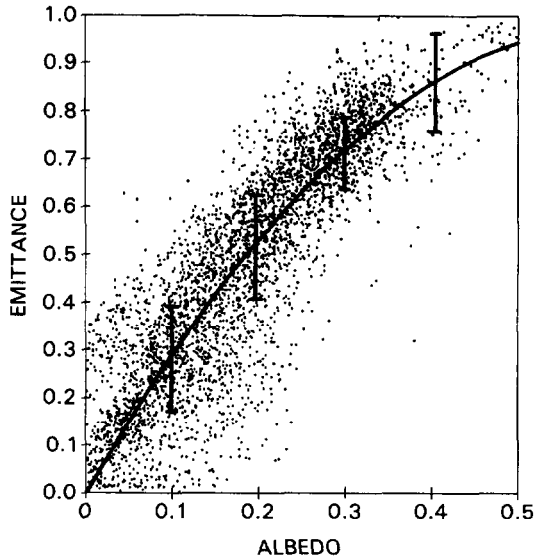

Figure 15 The effective emittance at 10.8 μm as a function of plane albedo at 0.75 μm for all measurements along the nadir track of the ER-2 on 28 October 1986. The curve represents a third-order polynomial fit to the observational data, and the error bars represent two standard deviations of the emittance averaged over 0.01 albedo intervals. (From Spinhirne and Hart, 1990.)

ship between nadir beam emittance and plane albedo. These results, presented in Fig. 15, were fitted to a third-order polynomial resulting in an expression of the following form:

$$\epsilon^{\uparrow}_{10.8} = 0.1456a^3_{0.75} - 2.677a^2_{0.75} + 3.185a_{0.75} \tag{9}$$

In this expression, strictly applicable for $0.0 \leq a_{0.75} \leq 0.45$, $\epsilon^{\uparrow}_{10.8}$ denotes the zenith-propagating beam emittance at 10.8 μm, and $a_{0.75}$ is the plane albedo at 0.75 μm. In addition to this parameterization, Spinhirne and Hart (1990) computed the standard deviation of the thermal beam emittance averaged over 0.01 albedo intervals, represented in Fig. 15 as error bars of one standard deviation on either side of the regression curve.

The relationship between visible reflectance and thermal emittance is also a major factor affecting the determination of cloud-top altitude and temperature from satellite observations. The thermal emittance determined by Spinhirne and Hart (1990) is decidedly less than that assumed by ISCCP for the global processing of satellite data at a given value of the visible reflectance (Rossow and Schiffer, 1991). This undoubtedly contributes to biases in the derivation of cloud-top altitude and temperature using ISCCP or NOAA-5 Scanning Radiometer (SR) algorithms (Rossow et al., 1989; Rossow and Schiffer, 1991), and points to the dire need to obtain further simultaneous observations of the spectral reflection and thermal emission properties of real clouds in a real atmosphere.

IV. Concluding Remarks

On examining the state of our knowledge of the radiative properties of clouds, we find that there has been a longstanding tendency for too many theories to chase too few observations. One of the most encouraging aspects of work carried out in recent years, which has been discussed in this review, is that increasing attention is being focused on new and innovative observational approaches and measurement techniques. These new approaches and instrumentation concepts make extensive use of both spectral and angular information, thus permitting greater examination of discrepancies between theory and observations than do traditional broadband flux observations. The growing use of cloud microphysics measurements to verify our interpretation of spectral cloud radiation observations is to be encouraged in the future.

Finally, it is important to recognize that much of the analysis that has thus far been applied to the remote sensing of cloud properties from aircraft and space-borne platforms has been based on applications of Mie theory for light scattering by spherical particles, and plane-parallel radiative transfer theory. There is a need to extend and revise these simple models, which are often able to explain the majority of the observed radiative properties of clouds, to problems associated with horizontal inhomogeneities in real clouds. These complexities have as yet not been fully explored using both theoretical calculations and experimental observations. This may very well limit the utility of many of the retrieval schemes discussed in this chapter to the special, simple cases to which they have thus far been applied.

References

Ackerman, S. A., and Cox, S. K. (1981). *J. Appl. Meteor.* **20**, 1510–1515.

Ackerman, S. A., Smith, W. L., Spinhirne, J. D., and Revercomb, H. E. (1990). *Mon. Wea. Rev.* **118**, 2377–2388.

Arking, A. (1991). *Bull. Amer. Meteor. Soc.* **71**, 795–813.

Arking, A., and Childs, J. D. (1985). *J. Climate Appl. Meteor.* **24**, 322–333.

Cess, R. D., Potter, G. L., Blanchet, J. P., Boer, G. J., Ghan, S. J., Kiehl, J. T., Le Treut, H., Li, Z. X., Liang, X. Z., Mitchell, J. F. B., Morcrette, J. J., Randall, D. A., Riches, M. R., Roeckner, E., Schlese, U., Slingo, A., Taylor, K. E., Washington, W. M., Wetherald, R. T., and Yagai, I. (1989). *Science* **245**, 513–516.

Cox, S. K., McDougal, D. S., Randall D. A., and Schiffer, R. A. (1987). *Bull. Amer. Meteor. Soc.* **68**, 114–118.

Curran, R. J., and Wu, M. L. C. (1982). *J. Atmos. Sci.* **39**, 635–647.

Curran, R. J., Kyle, H. L., Blaine, L. R., Smith, J., and Clem, T. D. (1981). *Rev. Sci. Instrum.* **52**, 1546–1555.

Davies, R., Ridgway, W. L., and Kim, K. E. (1984). *J. Atmos. Sci.* **41**, 2126–2137.

Foot, J. S., (1988). *Quart. J. Roy. Meteor. Soc.* **114**, 129–144.

Hansen, J. E., and Pollack, J. B. (1970). *J. Atmos. Sci.* **27**, 265–281.

Hansen, J. E., and Travis, L. D. (1974). *Space Sci. Rev.* **16**, 527–610.

Henyey, L. C., and Greenstein, L. J. (1941). *Astrophys. J.* **93**, 70–83.
Herman, B. M., Asous, W., and Browning, S. R. (1980). *J. Atmos. Sci.* **37**, 1828–1838.
Herman, G. F. (1977). *J. Atmos. Sci.* **34**, 1423–1432.
Herman, G. F., and Curry, J. A. (1984). *J. Climate Appl. Meteor.* **23**, 5–24.
Heymsfield, A. J., Miller, K. M., and Spinhirne, J. D. (1990). *Mon. Wea. Rev.* **118**, 2313–2328.
Hignett, P. (1987). *Quart. J. Roy. Meteor. Soc.* **113**, 1011–1024.
King, M. D. (1981). *J. Atmos. Sci.* **38**, 2031–2044.
King, M. D. (1987). *J. Atmos. Sci.* **44**, 1734–1751.
King, M. D., Strange, M. G., Leone, P., and Blaine, L. R. (1986). *J. Atmos. Oceanic Tech.* **3**, 513–522.
King, M. D., Radke, L. F., and Hobbs, P. V. (1990). *J. Atmos. Sci.* **47**, 894–907.
King, M. D., Kaufman, Y. J., Menzel, W. P., and Tanré, D. (1992). *IEEE. Trans. Geosci. Remote Sens.* **29**, 2–27.
Kneizys, K. X., Shettle, E. P., Gallery, W. O., Chetwynd, J. H., Abreu, L. W., Selby, J. E. A., Fenn, R. W. and McClatchey, R. A. (1980). Atmospheric transmittance/radiance: Computer code LOWTRAN 5. AFGL-TR-80-0067, Air Force Geophysics Laboratories, Hanscom AFB, 233 pp.
Kneizys, K. X., Shettle, E. P., Abreu, L. W., Chetwynd, J. H., Anderson, G. P., Gallery, W. O., Selby, J. E. A., and Clough, S. A. (1988). Users guide to LOWTRAN 7. AFGL-TR-88-0177, Air Force Geophysics Laboratories, Hanscom AFB, 137 pp.
Mel'nikova, I. N. (1978). *Izv. Acad. Sci., USSR, Atmos. Ocean. Phys.* **14**, 928–931.
Nakajima, T., and King, M. D. (1990). *J. Atmos. Sci.* **47**, 1878–1893.
Nakajima, T., King, M. D., Spinhirne, J. D., and Radke, L. F. (1991). *J. Atmos. Sci.* **48**, 728–750.
Newiger, M., and Bähnke, K. (1981). *Contr. Atmos. Phys.* **54**, 370–382.
Platt, C. M. R., Reynolds, D. W., and Abshire, N. L. (1980). *Mon. Wea. Rev.* **108**, 195–204.
Prabhakara, C., Fraser, R. S., Dalu, G., Wu, M. L. C., and Curran, R. J. (1988). *J. Appl. Meteor.* **27**, 379–399.
Prabhakara, C., Yoo, J. M., Dalu, G., and Fraser, R. S. (1990). *J. Appl. Meteor.* **29**, 1313–1329.
Ramanathan, V. (1987). *J. Geophys. Res.* **92**, 4075–4095.
Ramanathan, V., Pitcher, E. J., Malone, R. C., and Blackmon, M. L. (1983). *J. Atmos. Sci.* **40**, 605–630.
Ramanathan, V., Cess, R. D., Harrison, E. F., Minnis, P., Barkstrom, B. R., Ahmad, E., and Hartmann, D. (1989). *Science* **243**, 57–63.
Rawlins, F., and Foot, J. S. (1990). *J. Atmos. Sci.* **47**, 2488–2503.
Reynolds, D. W., Vonder Haar, T. H., and Cox, S. K. (1975). *J. Appl. Meteor.* **14**, 433–444.
Rossow, W. B., and Schiffer, R. A. (1991). *Bull. Amer. Meteor. Soc.* **72**, 2–20.
Rossow, W. B., Gardner, L. C., and Lacis, A. A. (1989). *J. Climate* **2**, 419–458.
Schiffer, R. A., and Rossow, W. B. (1983). *Bull. Amer. Meteor. Soc.* **64**, 779–784.
Slingo, A. (1989). *J. Atmos. Sci.* **46**, 1419–1427.
Slingo, A., and Schrecker, H. M. (1982). *Quart. J. Roy. Meteor. Soc.* **108**, 407–426.
Spinhirne, J. D., and Hart, W. D. (1990). *Mon. Wea. Rev.* **118**, 2329–2343.
Spinhirne, J. D., Hansen, M. Z., and Caudill, L. O. (1982). *Appl. Opt.* **21**, 1564–1571.
Spinhirne, J. D., Hansen, M. Z., and Simpson, J. (1983). *J. Climate Appl. Meteor.* **22**, 1319–1331.
Starr, D. O'C. (1987). *Bull. Amer. Meteor. Soc.* **68**, 119–124.
Stephens, G. L. (1978). *J. Atmos. Sci.* **35**, 2123–2132.
Stephens, G. L., and Platt, C. M. R. (1987). *J. Climate Appl. Meteor.* **26**, 1243–1269.
Stephens, G. L., and Tsay, S. C. (1990). *Quart. J. Roy. Meteor. Soc* **116**, 671–704.
Stephens, G. L., Paltridge, G. W., and Platt, C. M. R. (1978). *J. Atmos. Sci.* **35**, 2133–2141.
Stephens, G. L., Ackerman, S., and Smith, E. A. (1984). *J. Atmos. Sci.* **41**, 687–690.
Stowe, L. L., Yeh, H. Y. M., Eck, T. F., Wellemeyer, C. G., Kyle, H. L., and the Nimbus-7 Cloud Data Processing Team (1989). *J. Climate* **2**, 671–709.
Taylor, J. P. (1992). *J. Atmos. Sci.* **49**, 2564–2569.
Twomey, S. (1972). *J. Atmos. Sci.* **29**, 1156–1159.

Twomey, S. (1976). *J. Atmos. Sci.* **33**, 1087–1091.
Twomey, S. (1977). *J. Atmos. Sci.* **34**, 1149–1152.
Twomey, S. (1983). *Contrib. Atmos. Phys.* **56**, 429–439.
Twomey, S., and Cocks, T. (1982). *J. Meteor. Soc. Japan* **60**, 583–592.
Twomey, S., and Cocks, T. (1989). *Beitr. Phys. Atmos.* **62**, 172–179.
Welch, R. M., Cox, S. K., and Davis, J. M. (1980). *Solar Radiation and Clouds*. Meteor. Monogr. No. 39, *Amer. Meteor. Soc.*, 96 pp.
Wielicki, B. A., Suttles, J. T., Heymsfield, A. J., Welch, R. M., Spinhirne, J. D., Wu, M. L. C., Starr, D. O'C., Parker, L., and Arduini, R. F. (1990). *Mon. Wea. Rev.* **118**, 2356–2376.
Wiscombe, W. J., Welch, R. M., and Hall, W. D. (1984). *J. Atmos. Sci.* **41**, 1336–1355.
Wu, M. L. C. (1987). *J. Appl. Meteor.* **26**, 225–233.

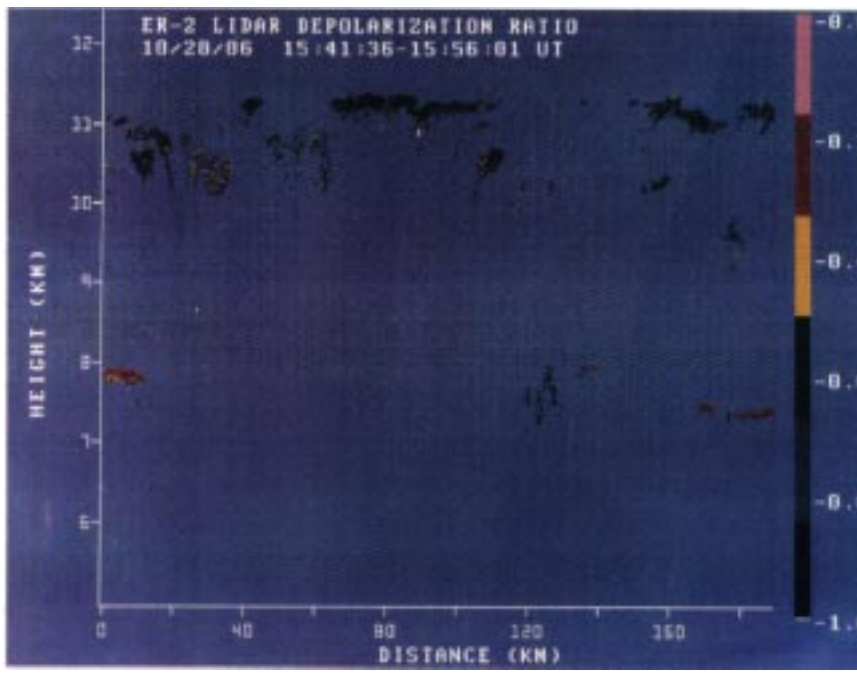

Plate 1. Lidar depolarization ratio as a function of altitude and distance along the nadir track of the ER-2 on 28 October 1986. The depolarization ratio for the upper cloud layer and the lower diffuse cloud at 120 km is large, due primarily to the presence of ice crystals. The thin altocumulus layer having a low depolarization ratio consists primarily of supercooled water droplets. (From Spinhirne and Hart, 1990.)

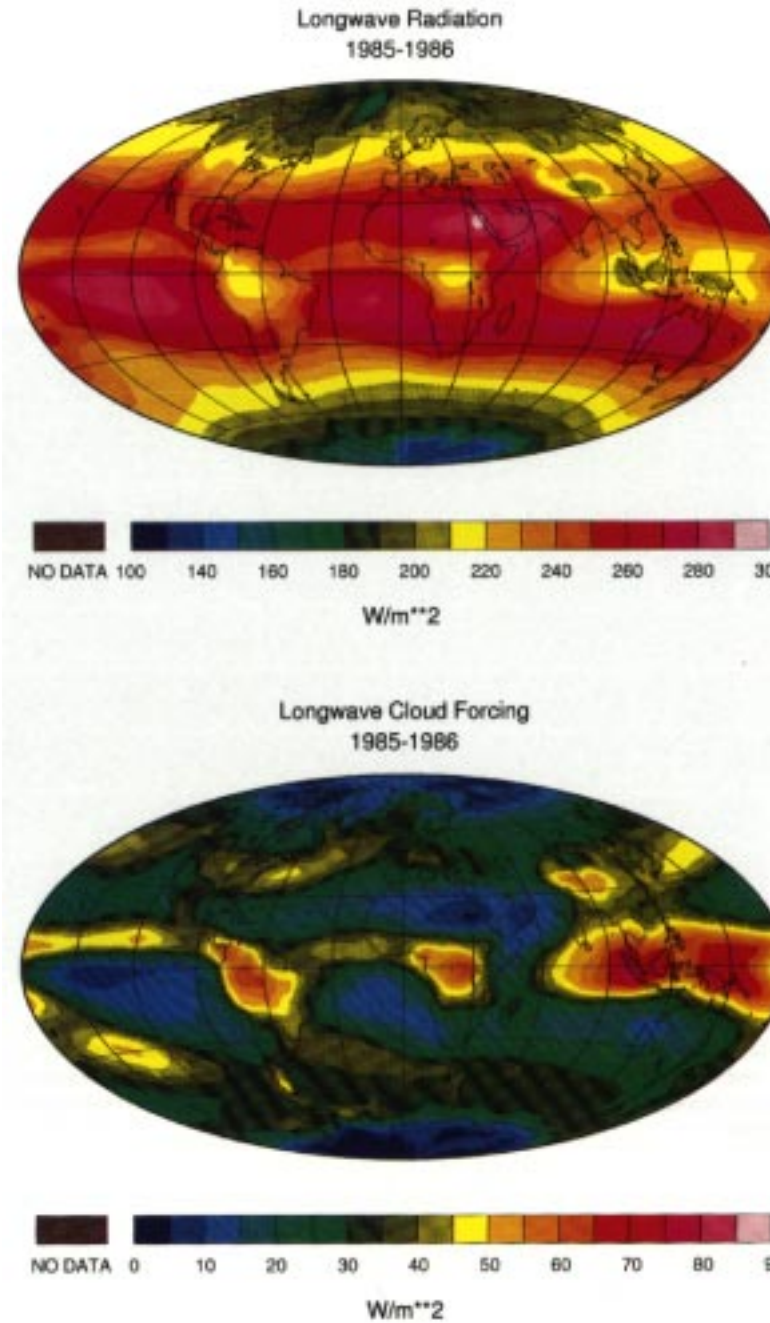

Plate 2. Annual average outgoing longwave radiation (top) and longwave cloud radiative forcing (bottom) determined from two years (1985-1986) of ERBE scanner data on the ERBS and NOAA-9 satellites.

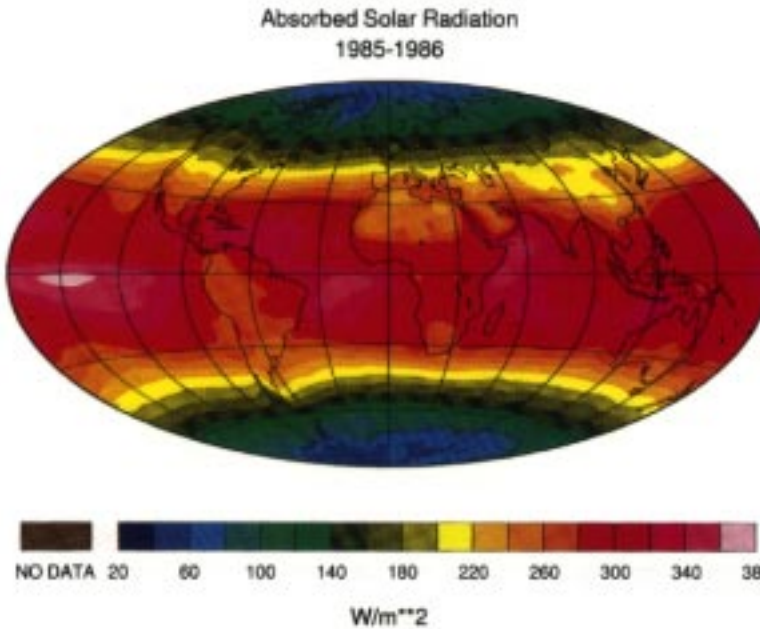

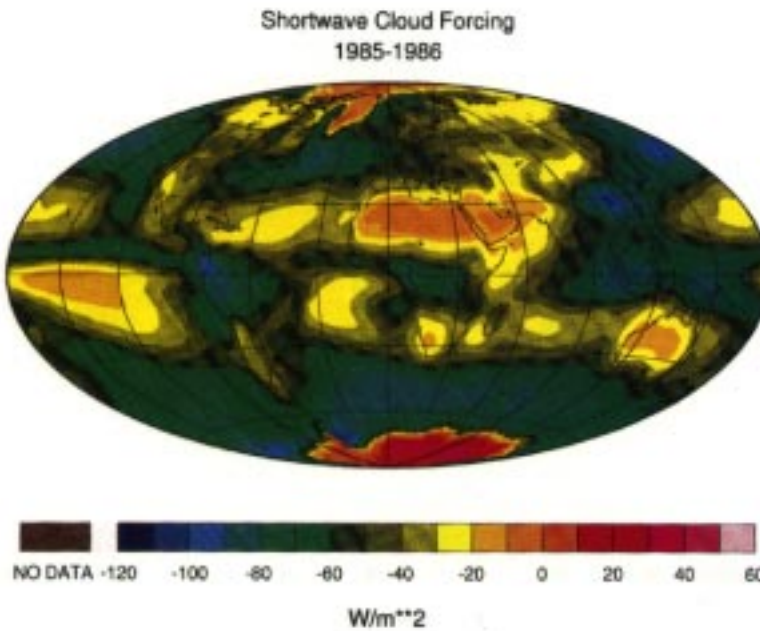

Plate 3. Annual average absorbed solar radiation (top) and shortwave cloud forcing (bottom) determined from two years (1985-1986) of ERBE scanner data on the ERBS and NOAA-9 satellites.

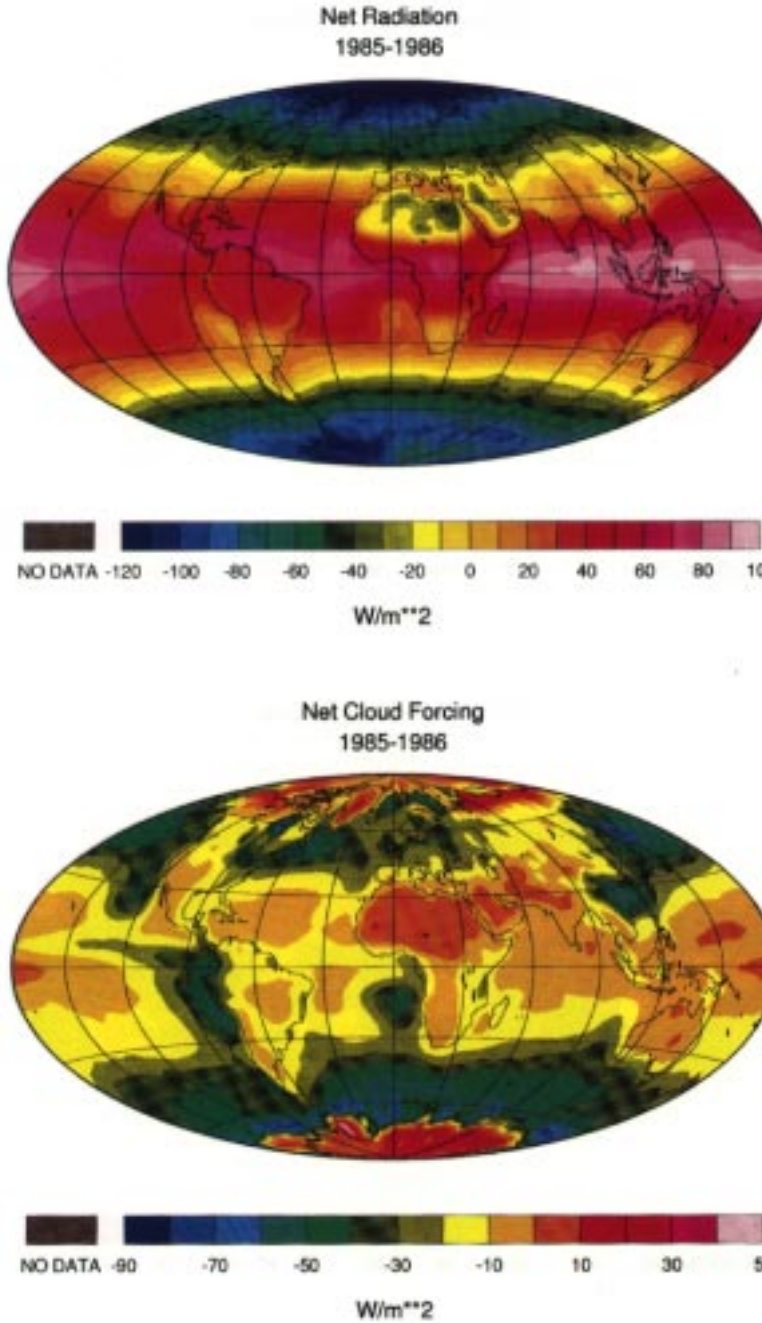

Plate 4. Annual average net radiation (top) and net cloud radiative forcing (bottom) determined from two years (1985-1986) of ERBE scanner data on the ERBS and NOAA-9 satellites.

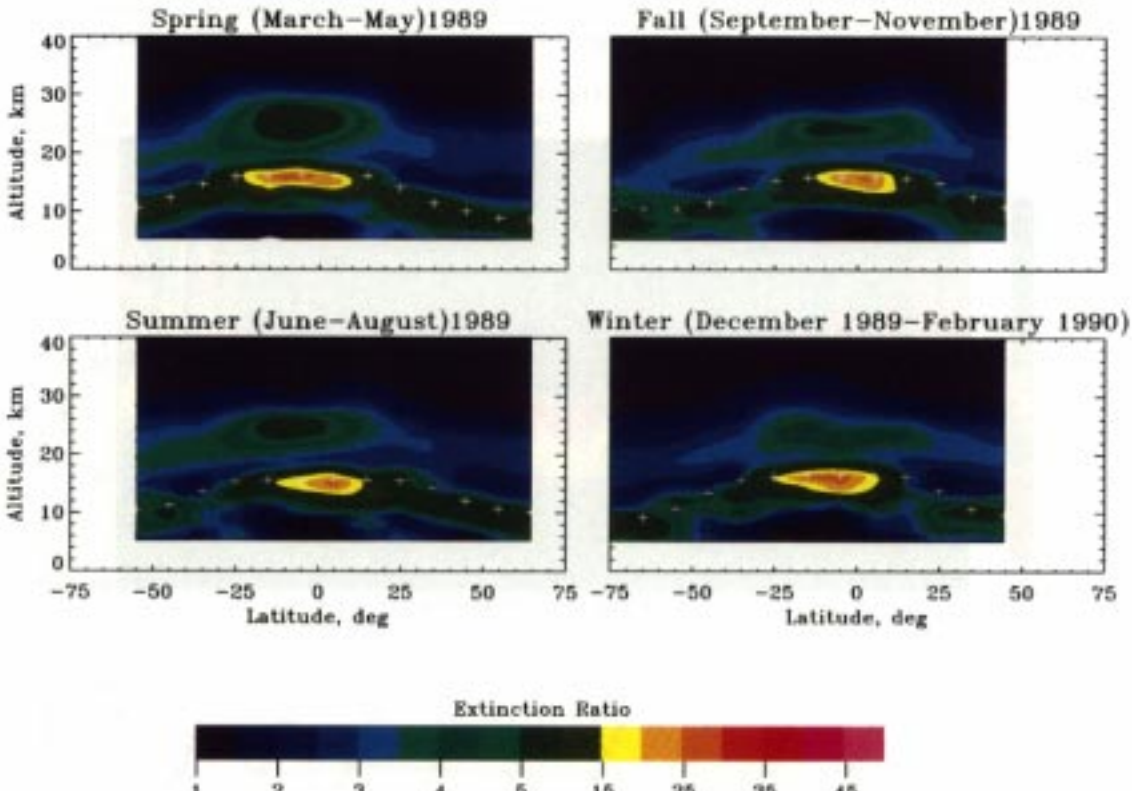

Plate 5. Seasonally averaged zonal mean aerosol extinction ratio (i.e., ratio of aerosol extinction coefficient to molecular extinction coefficient) for 1989 northern hemisphere spring (March–May), summer (June–August), fall (September–November), and winter (December 1989–February 1990). Measurements from SAGE II.

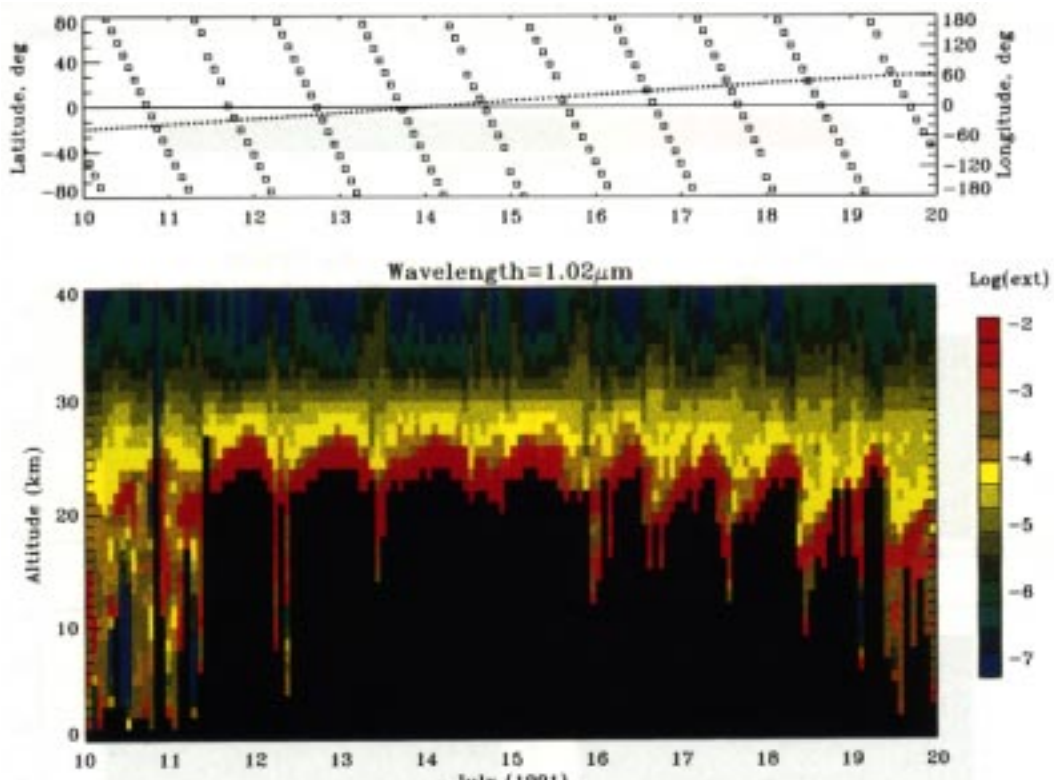

Plate 6. Time series of the SAGE II aerosol extinction profile measurements at 1.02-μm wavelength for July 10–20, 1991. Dots represent latitude; solid squares represent longitude.

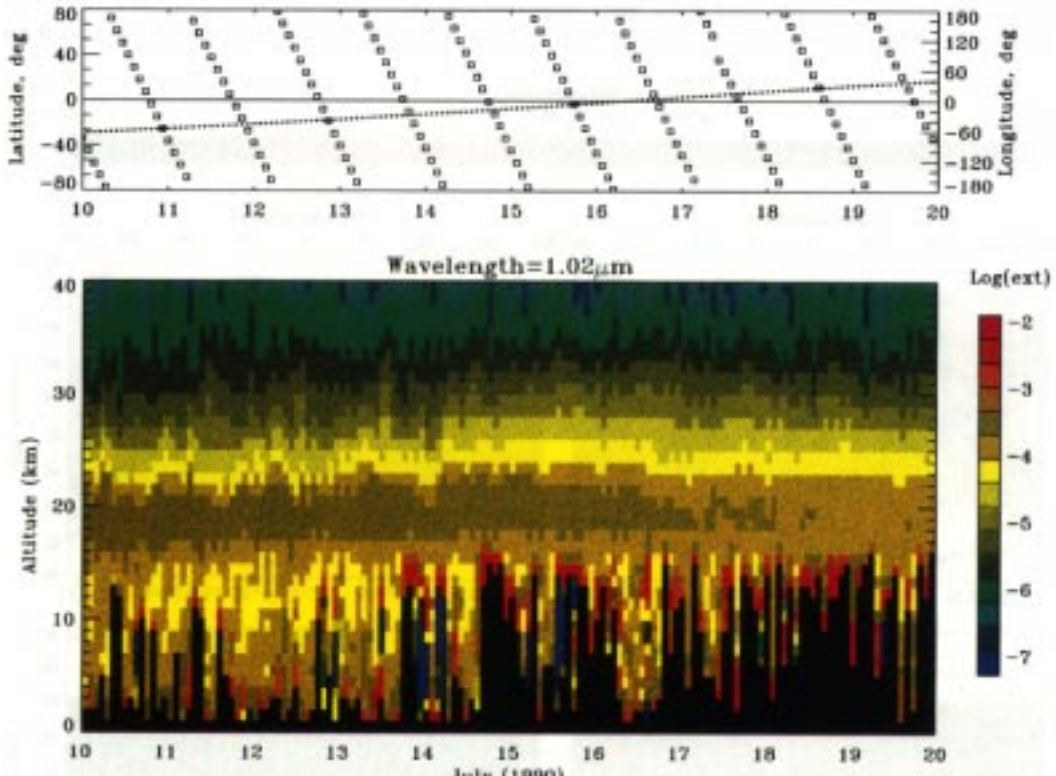

Plate 7. Time series of the SAGE II aerosol extinction profile measurements at 1.02-μm wavelength for July 10–20, 1990. Dots represent latitude; solid squares represent longitude.

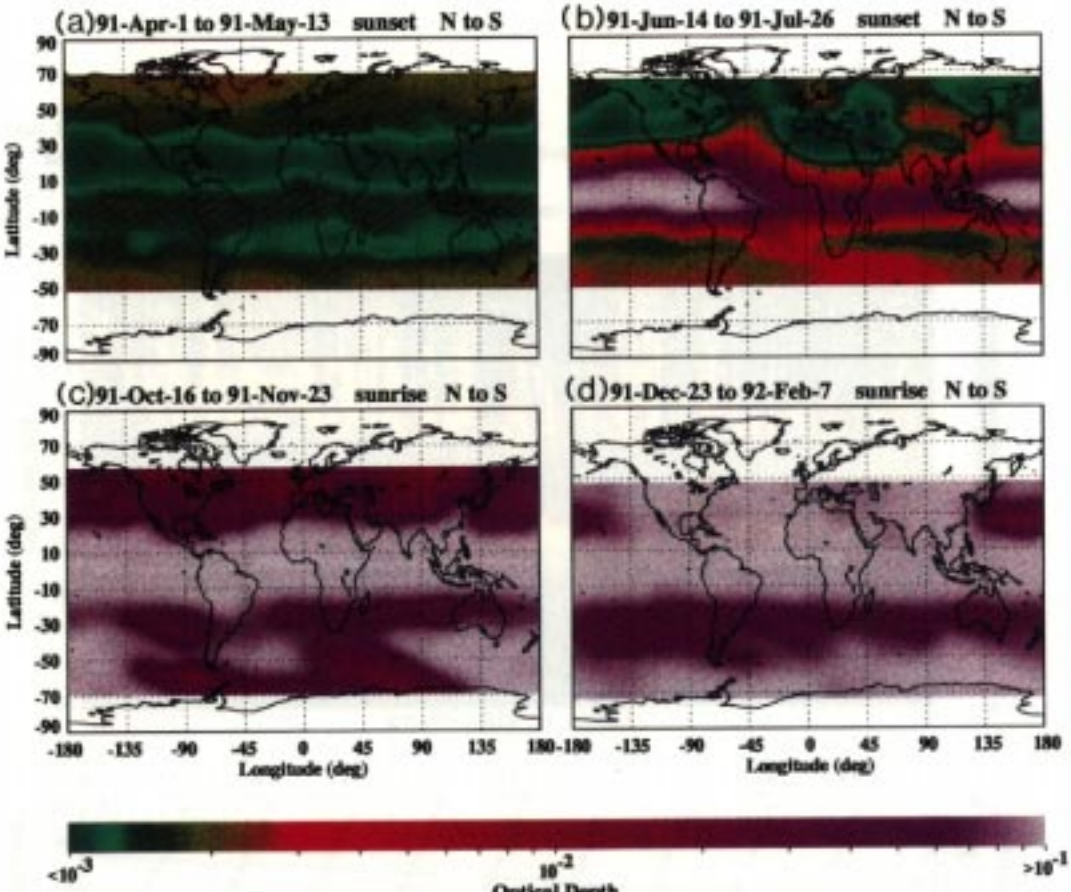

Plate 8. Longitude–latitude distributions of SAGE II 1.02-μm stratospheric aerosol optical depth: (a) April 1, 1991, to May 13, 1991; (b) June 14, 1991, to July 26, 1991; (c) October 16, 1991, to November 23, 1991; and (d) December 23, 1991, to February 7, 1992.